J. Fluid Mech. (2025), *vol*. 1004, A15, doi:10.1017/jfm.2024.1172

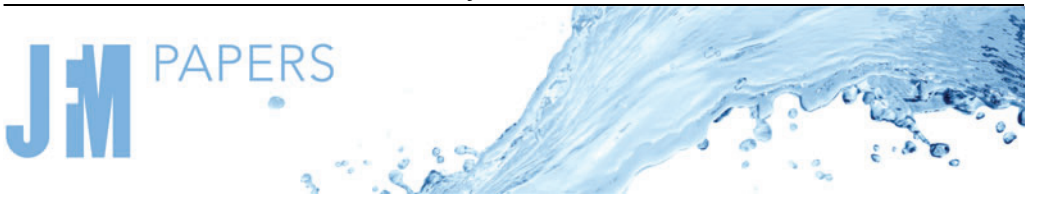

Direct numerical simulation study of turbulent pipe flow with imposed radial rotation

Alessandro Ceci[1],† **and Sergio Pirozzoli**[1]

[1]Dipartimento di Ingegneria Meccanica ed Aerospaziale, Sapienza University of Rome, Via Eudossiana 18, 00184 Rome, Italy

(Received 12 March 2024; revised 30 November 2024; accepted 3 December 2024)

We carry out direct numerical simulations (DNS) of fully developed turbulent pipe flow subjected to radial system rotation, examining a broad range of rotational speed and Reynolds number. In response to the imposed system rotation, strong secondary motions arise in the form of streamwise-aligned counter-rotating eddies, which engage significantly with the boundary layer, exerting a notable influence on the turbulent flow. At high rotation numbers, a Taylor–Proudman region appears, marked by a constant mean axial velocity along the rotation axis. As rotation increases, local flow relaminarisation takes place starting at the suction side of the pipe, ultimately resulting in full relaminarisation when the rotation number is higher than unity. In this regime the near-wall region of the flow exhibits the typical hallmark of laminar Ekman layers, whose strength varies with the azimuthal position along the pipe perimeter. A predictive analytical formula for frictional drag is derived for this ultimate high rotation which accurately reproduces the DNS data. The behaviour of friction is more complex to predict at low-to-intermediate rotation numbers owing to concurrent effects of viscosity, turbulence, secondary motions and rotation, which we quantify in an extended version of the Fukagata–Iwamoto–Kasagi identity.

Key words: pipe flow, turbulence simulation, rotating flows

1. Introduction

Flows in rotating passages are prevalent in technological applications, especially in turbomachinery (Greitzer, Tan & Graf 2007). In pipe flow, two canonical cases can be identified, in which the rotation axis is either parallel or orthogonal to the pipe axis. In the latter case on which we focus in the present work, Coriolis forces act on the fluid as body

† Email address for correspondence: alessandro.ceci@uniroma1.it

forces, breaking the azimuthal symmetry of the flow and inducing large-scale secondary motions in the cross-stream plane. In particular, turbulence is suppressed at the suction side of the duct, and enhanced at the pressure side, as highlighted in research dealing with rotating channels (Kristoffersen & Andersson 1993). In a pioneering work, Barua (1954) studied analytically laminar pipe flows with imposed radial rotation, obtaining estimates for the friction coefficient. However, no such theory exists for the case where the baseline pipe flow is turbulent, which makes it a compelling research case. Benton & Boyer (1966) studied the flow through rapidly rotating channels of various cross-section, from the experimental and analytical standpoint. For very high rotation rates, they showed that the significance of viscous effects is confined to thin boundary layers along the channel walls. Solutions for both the geostrophic region and the boundary layers were derived and integrated to yield the entire velocity field. Experimental findings for a circular conduit were provided, demonstrating favourable consistency with the theoretical framework.

Ito & Nanbu (1971) investigated experimentally friction in fully developed smooth pipe flow radially rotating at a constant angular velocity for bulk Reynolds numbers in the range from 20 to 60 000, presenting empirical predictions for the friction factor in both laminar and turbulent flow. Johnston, Halleent & Lezius (1972) conducted experimental investigations on fully developed turbulent channel flow under steady rotation about a spanwise axis. They found that the Coriolis force components in the region of two-dimensional mean flow impacted both local and global stability.

Kristoffersen & Andersson (1993) conducted direct numerical simulation (DNS) of fully developed pressure-driven turbulent flow in a rotating channel at a fixed low Reynolds number, for various rotational speeds. At the lowest rotational speed, turbulence statistics were found to be barely affected, with opposite effects observed along the stable suction side and the unstable pressure side. Turbulent Reynolds stresses were found to decrease near the suction side at increasing rotational speed, whereas turbulence intensities increased on the pressure side, with streamwise intensity and the Reynolds shear stress also increasing at moderate rotational speed but suppressed at higher speed. The mean velocity profile was found to become increasingly asymmetric at high rotational speeds, reflecting experimental observations. Large-scale coherent structures were deemed to be responsible for transporting highly turbulent fluid from the pressure side to the channel middle, enhancing the turbulence levels. However, those structures were unstable for most rotation cases considered. Using similarity arguments and leveraging experimental and numerical data, Ishigaki (1996) demonstrated quantitative analogy between fully developed turbulent flows in curved pipes and orthogonally rotating pipes.

Large-eddy simulations of turbulent flow in a rotating square duct at fixed low Reynolds number were carried out by Pallares & Davidson (2000). Notable changes from the non-rotating state were observed even at low rotation rates, driven by the secondary motions near the duct corners. The Coriolis effect was found to generate a descending cross-stream current in the duct core, enhancing streamwise vorticity and secondary motions that convect upwards near the sidewalls and towards the duct centre. Rotation was found to intensify turbulence near walls where the main shear vorticity aligns with the background vorticity, and to reduce turbulence at the other walls. At the highest rotation rate considered by those authors, the turbulence levels were found to decrease at the stable side due to flow stabilisation into a Taylor–Proudman regime resulting from intensified Coriolis-induced vertical convective transport of streamwise momentum. In a follow-up study, Pallares, Grau & Davidson (2005) derived a predictive formula for the velocities and friction coefficients in a rotating square duct based on the solution of the simplified set of

momentum equations. At rotational speed, the Ekman layers were found to be responsible for a large share of the pressure drop.

Experimental investigations of rapidly rotating turbulent square and rectangular duct flows were conducted by Mårtensson *et al.* (2002), at low-to-moderate Reynolds number. Examination of inclined duct flow confirmed the significance of the normal component of the rotation vector in understanding rotational effects. Analysis of various duct geometries indicated that the contribution to pressure drop from near-wall Ekman layers dominated, yielding an increase of the friction coefficient with the rotational speed. Rotation effects were also studied by Dai *et al.* (2015) and Fang *et al.* (2017) for square ducts and by Rosas, Zhang & Wang (2021) for elliptical pipes. At moderate rotation rate, the suction side was found to relaminarise first as Coriolis forces dominate the energy transfer mechanisms, and a Taylor–Proudman region was observed at high rotation numbers. The DNS of radially rotating turbulent pipe flow by Zhang & Wang (2019) revealed asymmetric flow patterns, with high-speed flow on the pressure side of the pipe and low-speed flow on the suction side, driven by Coriolis forces. Secondary motions were observed to emerge, which eventually disappear at high enough rotational speed. Those authors also found that the Coriolis force affected the budget of Reynolds shear stress, leading to asymmetric profiles and a decrease of Reynolds stresses at increasing rotational speed.

The key controlling parameter in rotating duct flow is the rotation number, defined as the ratio of a typical rotation velocity (e.g. angular velocity by hydraulic diameter) to the flow bulk velocity. Typical rotation numbers in turbomachinery applications are in the range 0.3–0.38, as documented in the studies of Coletti *et al.* (2012, 2014). Higher rotation rates are nevertheless significant in various engineering applications, particularly in gas turbine engines, for which the rotation number can be as high as 3.33–10 (Atkins & Kanjirakkad 2014; Jackson *et al.* 2021; Luberti *et al.* 2021; Visscher *et al.* 2011; Sun *et al.* 2022). Furthermore, experimental studies of cooling systems such as that of Morris (1996) emphasise the relevance of rotation numbers of about two in typical engine conditions, at which the cooling performance is severely affected from secondary flows generated by Coriolis forces. Liou *et al.* (2007) numerically simulated duct flow with rotation number in the range between zero and two, and asserted that there is a strategic need to extend the experimental data to emulate more closely realistic engine conditions by extending Reynolds number and rotation number simultaneously. This shortcoming is also well portrayed in the study of Ligrani (2013).

Given this background, is is clear that there is a strong demand for improving the knowledge of flows in ducts in the presence of rotation, since: (1) existing DNS and large-eddy simulations are restricted to low Reynolds number, at which turbulence is barely developed; (2) experimental measurements are scarce, and by the way affected by substantial uncertainties; (3) there is a lack of data for the technologically outstanding case of flow in a rotating circular pipe; and (4) predictive friction formulas for duct flow are not sufficiently qualified, and mainly based on empirical fitting of existing (sparse) data. The goal of this work is then to fill in the existing gap of knowledge, and for that purpose we carry out DNS of flow in a smooth circular pipe subjected to radial rotation, at sufficiently high Reynolds number to be representative of realistic flow instances, and for a wide range of rotation numbers. The paper is organised as follows. In § 2 we present the DNS dataset used for the analysis. The flow structure and the turbulence statistics are presented in § 3, and friction is analysed in detail in § 5. Concluding comments are made in § 6.

2. The numerical dataset

The DNS solver relies on a second-order finite-difference discretisation of the incompressible Navier–Stokes equations in cylindrical coordinates, utilising the marker-and-cell method to maintain discrete conservation of the total kinetic energy (Orlandi 2000). To ensure a constant mass flow rate, uniform volumetric forcing is applied to the axial momentum equation. The Poisson equation resulting from enforcement of the divergence-free condition is efficiently solved through double trigonometric expansion in periodic axial and azimuthal directions, coupled with tridiagonal matrix inversion in the radial direction (Kim & Moin 1985). The polar singularity at the pipe axis is handled as suggested by Verzicco & Orlandi (1996). Time advancement relies on a hybrid third-order low-storage Runge–Kutta algorithm, whereby diffusive terms are treated implicitly and convective terms are treated explicitly. Implicit treatment of the convective terms in the azimuthal direction is also used to mitigate the time-step restriction (Akselvoll & Moin 1996; Wu & Moin 2008). The code is optimised for GPU clusters using CUDA Fortran and OpenACC directives, with CUFFT libraries facilitating fast Fourier transforms (Fatica & Ruetsch 2014).

A sketch of the computational domain is shown in figure 1. The radial coordinate measured from the pipe axis is denoted as r. Numerical simulations are carried out using periodic boundary conditions in the axial (z) and azimuthal (θ) directions. The effect of rotation is accounted for by augmenting the Navier–Stokes equations with the Coriolis forces:

$$\boldsymbol{F}_c = 2\Omega \begin{bmatrix} -u_z \sin\theta \\ u_z \cos\theta \\ u_r \cos\theta - u_\theta \sin\theta \end{bmatrix}, \tag{2.1}$$

where the angular velocity (Ω) is assumed to be parallel to the polar (x_2) axis. The wall distance is hereafter denoted as y. As noted in previous studies, centrifugal forces are not explicitly added as they are absorbed into the pressure term (Kristoffersen & Andersson 1993). As illustrated in figure 1, the primary effect of rotation normal to the pipe axis is the onset of Coriolis forces which on average act orthogonal to both the pipe axis and the rotation axis, resulting in increased shear at the pressure side of the pipe and in shear suppression at the suction side. The flow is controlled by two parameters, namely the bulk Reynolds number, $Re_b = 2Ru_b/\nu$, and the rotation number, $N = \Omega R/u_b$, with R the pipe radius, u_b the bulk velocity and ν the fluid kinematic viscosity. This definition is used here as it emphasises the maximum peripheral velocity with respect to the bulk velocity, but one should be careful and note that several previous studies of rotating ducts rather define the rotation number based on the hydraulic diameter, here the pipe diameter. The friction Reynolds number Re_τ is also an important flow parameter, defined as $Re_\tau = Ru_\tau^*/\nu$, with $u_\tau^* = (\tau_w^*/\rho)^{1/2}$ the global friction velocity and τ_w^* the azimuthally averaged mean wall shear stress. The flow properties normalised by these global viscous scales are hereafter denoted with an asterisk. In all DNS the pipe length is taken to be $L_z = 15R$, which we have found to be sufficient to achieve convergence of all the statistics herein reported, as shown in the Appendix. The grid points are clustered towards the pipe walls according to the stretching function developed by Pirozzoli & Orlandi (2021), whereas the grid points are uniformly spaced in the z and θ directions. Adequacy of the grid resolution has been evaluated through a grid sensitivity analysis, also reported in the Appendix.

A complete list of the simulations that we have carried out is given in table 1. A one-decade range of Reynolds numbers has been explored, along with a wide range of rotation numbers, including cases with weak rotation as well as cases in which

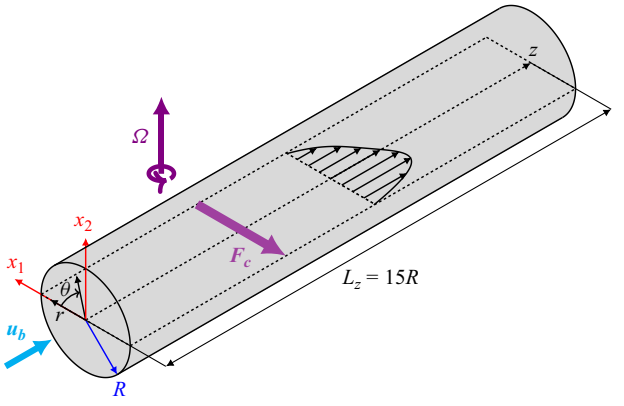

Figure 1. Definition of coordinate system for DNS of rotating pipe flow. Coordinates z, r, θ are the axial, radial and azimuthal coordinates, respectively, R is the pipe radius, L_z is the pipe length, u_b is the bulk velocity, $\boldsymbol{\Omega}$ is the angular velocity and $\boldsymbol{F}_c$ is the resultant mean Coriolis force. The Cartesian coordinates x_1, x_2 define positions in the cross-stream plane.

rotation dominates. For the sake of clarity, uppercase letters are used to denote flow properties averaged along the axial direction and in time, and fluctuations thereof are denoted with lowercase letters. Instantaneous properties are denoted with tilde superscripts. Angular brackets are used to denote the averaging operator.

3. Flow organisation

As a first step, we analyse the flow organisation from representative instantaneous snapshots at the two extreme Reynolds numbers, namely $Re_b = 17\,000$ and $Re_b = 133\,000$. Specifically, in figures 2 and 3 we show the contours of the axial velocity in the cross-stream plane and in figures 4 and 5 we show the axial velocity contours in a cylindrical shell at small distance ($y^* = 15$ for the non-rotating case) from the wall. The former are used to get insight into the large-scale bulging motions which connect the near-wall region with the bulk flow, whereas the latter are used to get insight into the modifications of the near-wall streaks resulting from pipe rotation. For the sake of correct interpretation of the figures, we note that the azimuth angle θ as defined in figure 1 is such that $\theta = 0^\circ \pm 15^\circ$ corresponds to the suction side of the pipe, whereas $\theta = 180^\circ \pm 15^\circ$ corresponds to pressure side. Coriolis forces are such that on average momentum is transported from the suction side towards the pressure side (Zhang & Wang 2019). The angles $\theta = 90^\circ$ and 270° correspond to the north and south poles of the pipe, respectively, along which the effects of rotation are most active. The first important information gained from the visualisations is that, even at modest rotation number (less that about 0.01) the effect of rotation is quite apparent on the suction side, which shows a visible momentum defect with respect to the pressure side. Bulging motions are instead still observed on the rest of the pipe perimeter. As the rotation number increases, the zone with reduced momentum at the suction side of the pipe becomes progressively more extended, and severe reduction of the turbulence activity is visible at $N \gtrsim 0.1$. At higher rotation numbers suppression of turbulence is also visible within the pipe core, and hints of flow relaminarisation become visible also on the pressure side at $N \gtrsim 1$. Eventually, at high rotation rates, the flow tends to become symmetric about the polar axis, and the velocity field tends to become organised in bands parallel to it. The relaminarisation process is best observed in the near-wall shells. At low rotation numbers streaks dominate

Re_b	Re_τ	N	N_τ	$N_z \times N_r \times N_\theta$	$N_{5\Delta}$	$\lambda \times 10^{-2}$	Line
17 000	496	0.0009765625	0.0167	769 × 97 × 769	97	2.72	—
17 000	497	0.001953125	0.0334	769 × 97 × 769	97	2.73	—
17 000	501	0.00390625	0.0663	769 × 97 × 769	91	2.78	—
17 000	509	0.0078125	0.130	769 × 97 × 769	75	2.87	—
17 000	516	0.015625	0.257	769 × 97 × 769	62	2.94	—
17 000	523	0.03125	0.507	769 × 97 × 769	53	3.03	
17 000	539	0.0625	0.986	769 × 97 × 769	45	3.21	
17 000	566	0.125	1.87	769 × 97 × 769	39	3.56	
17 000	610	0.25	3.48	769 × 97 × 769	35	4.12	
17 000	669	0.5	6.34	769 × 97 × 769	31	4.96	
17 000	856	2.0	19.8	769 × 97 × 769	24	8.12	
17 000	1004	4.0	33.8	769 × 97 × 769	22	11.2	
17 000	1187	8.0	57.2	769 × 97 × 769	19	15.6	
44 000	1188	0.01	0.185	1793 × 165 × 1793	84	2.33	—
44 000	1296	0.1	1.69	1793 × 165 × 1793	48	2.78	—
44 000	1405	0.5	7.83	1793 × 165 × 1793	35	3.26	—
44 000	1761	2.0	25.0	1793 × 165 × 1793	27	5.12	—
44 000	2043	4.0	43.0	1793 × 165 × 1793	24	6.90	—
44 000	2418	8.0	72.7	1793 × 165 × 1793	22	9.67	—
82 500	2077	0.01	0.198	3073 × 244 × 3073	97	2.03	—
82 500	2294	0.1	1.79	3073 × 244 × 3073	53	2.47	—
82 500	2379	0.5	8.66	3073 × 244 × 3073	38	2.66	—
82 500	2833	2.0	29.1	3073 × 244 × 3073	29	3.77	—
82 500	4595	16.0	143	3073 × 244 × 3073	21	9.93	—
133 000	3181	0.01	0.209	4609 × 328 × 4609	107	1.83	—
133 000	3527	0.1	1.88	4609 × 328 × 4609	57	2.25	
133 000	3663	0.5	9.15	4609 × 328 × 4609	40	2.39	
133 000	4110	2.0	32.3	4609 × 328 × 4609	31	3.06	
133 000	6573	16.0	161	4609 × 328 × 4609	22	7.82	

Table 1. Flow parameters for DNS of rotating pipe flow. The bulk Reynolds number is defined as $Re_b = 2Ru_b/\nu$, with R the pipe radius, u_b the bulk velocity and ν the fluid kinematic viscosity; $N = \Omega R/u_b$ is the rotation number and $N_\tau = \Omega R/u_\tau^*$ is the friction rotation number with the global friction velocity. Parameters N_z, N_r, N_θ are respectively the number of grid points in the axial, radial and azimuthal directions. The parameter $N_{5\Delta}$ highlights the number of points in the radial direction up to five Ekman layer thicknesses $\Delta = (\nu/\Omega)^{1/2}$, evaluated at $\theta = \pm 90^\circ$. The global friction factor is $\lambda = 8\tau_w^*/\rho u_b^2$, with τ_w^* the azimuthally averaged mean wall shear stress and ρ the fluid density. Parameter $Re_\tau = Ru_\tau^*/\nu$ is the friction Reynolds number, with $u_\tau^* = (\tau_w^*/\rho)^{1/2}$ the mean friction velocity.

the near-wall region, although some evidence for their local suppression at $\theta \approx 0^\circ$ is visible. At intermediate rotation numbers streaks become progressively confined about the poles of the pipe, and they tend to vanish on the pressure side as well. At high rotation numbers, the flow no longer shows any sign of turbulence activity (please see supplementary movies at: https://doi.org/10.1103/APS.DFD.2023.GFM.V0041).

Since the flow exhibits homogeneity in the axial direction, its statistical characteristics solely rely on the azimuthal and radial coordinates. The mean axial velocity within the cross-stream plane is depicted in figure 6 for flow cases with $Re_b = 17\,000$, at various rotation numbers. Representative cross-flow streamlines are superimposed to the velocity contours to emphasise the variations in secondary motions as the rotation number changes. At low-to-moderate N (figure 6*a–d*), a notable alteration involves the symmetry breaking with respect to the polar axis, which implies gradual increase of axial

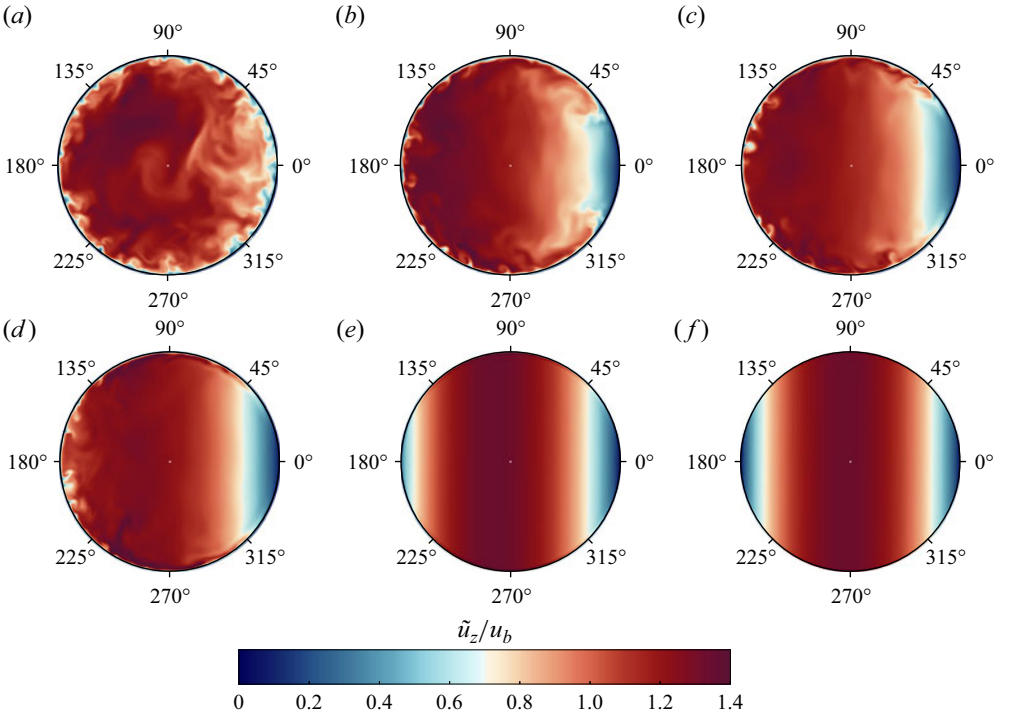

Figure 2. Instantaneous axial velocity contours at $Re_b = 17\,000$ in the cross-stream plane. Contour levels ranging from 0 to 1.4 are shown, in colour scale from blue to red. The pressure side of the pipe is on the left and the suction side is on the right of each panel. Various rotation numbers are considered: (*a*) $N = 0.0078125$, (*b*) $N = 0.125$, (*c*) $N = 0.25$, (*d*) $N = 0.5$, (*e*) $N = 2.0$, (*f*) $N = 8.0$.

momentum on the pressure side of the pipe (left) and a decrease on the suction side (right), on account of Coriolis forces. Consequently, secondary motions emerge in the form of two counter-rotating eddies that facilitate momentum redistribution across the pipe cross-section, with primary flow moving from the suction to the pressure side along the horizontal symmetry axis and return motion occurring along the circumference of the pipe. Remarkably, at low N, these secondary motions closely resemble those predicted to form under laminar flow conditions (Barua 1954). As the rotation number increases, there is a discernible trend towards uniformity in mean velocity along the vertical direction, accompanied by a tendency for the momentum deficit at the suction to be compensated, resulting in symmetrisation of the flow field. This observed phenomenon distinctly marks the onset of Taylor–Proudman columns (Proudman 1916; Taylor 1917), characterised by a tendency for the velocity to be constant along the axis of rotation, with no tilting or stretching of material lines parallel to this axis. At extreme rotation numbers, the secondary motions correspondingly take the form of right-to-left cross-stream motion, with return motions barely noticeable and confined to the near-wall proximity. Identical cross-stream flow information is presented in figure 7 for flow cases with $Re_b = 133\,000$. A remarkably similar flow pattern is discerned at corresponding values of the rotation number, for instance, comparing figure 6(*a*,*d*) with figure 7(*a*,*b*). This observation reinforces the idea that rotational effects on the mean flow properties are relatively unaffected by changes in the flow Reynolds number.

Due to the rearrangement of the flow, significant changes occur in wall friction as N varies. To examine this effect, figure 8 illustrates the local streamwise wall shear stress,

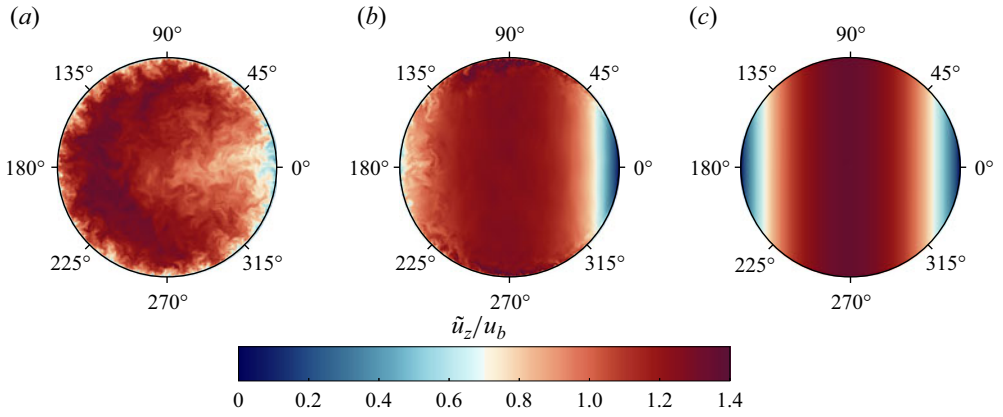

Figure 3. Instantaneous axial velocity contours at $Re_b = 133\,000$ in the cross-stream plane. Contour levels ranging from 0 to 1.4 are shown, in colour scale from blue to red. The pressure side of the pipe is on the left and the suction side is on the right of each panel. Various rotation numbers are considered: (*a*) $N = 0.01$, (*b*) $N = 0.5$, (*c*) $N = 16.0$.

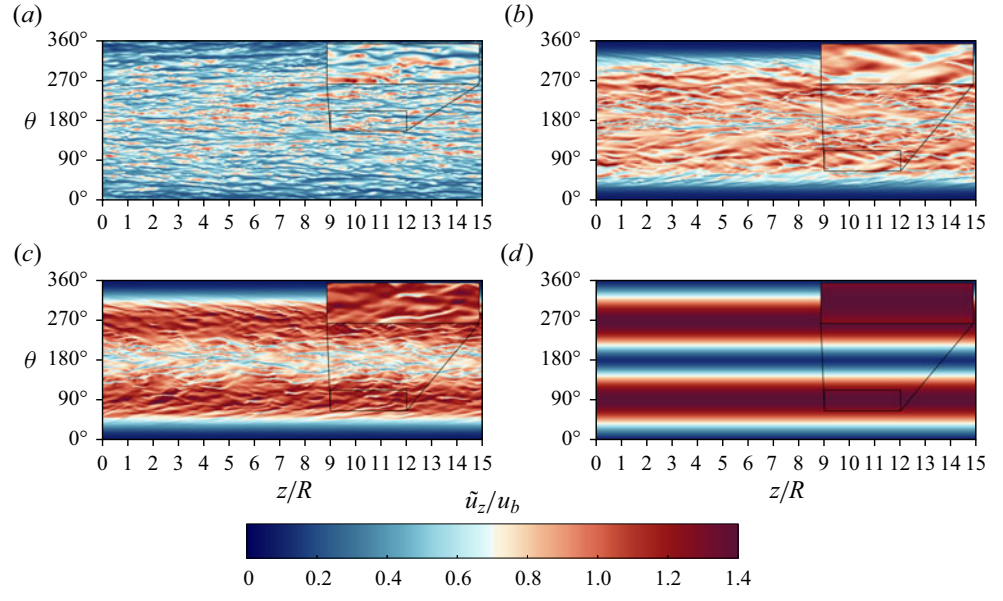

Figure 4. Instantaneous axial velocity contours at $Re_b = 17\,000$ in an unrolled cylindrical shell at a distance $y^* = 15$ from the wall (evaluated in the non-rotating case). Contour levels ranging from 0 to 1.4 are shown, in colour scale from blue to red. The insets in the top-right corner of each panel report magnified views of a small portion of the shell. Various rotation numbers are considered: (*a*) $N = 0.0078125$, (*b*) $N = 0.25$, (*c*) $N = 0.5$, (*d*) $N = 8.0$.

$\tau_w/\rho = \nu \partial U_z/\partial y|_w$, normalised either by the reference dynamic pressure ρu_b^2 (figure 8*a*,*c*) or the mean wall shear stress τ_w^* (figure 8*b*,*d*). A polar diagram is employed for clarity. The figure clearly demonstrates that even at very low rotational speeds, friction is nearly completely suppressed at the suction side of the pipe ($\theta = 0$). Conversely, the behaviour on the pressure side ($\theta = \pi$) is non-monotonic, where the local streamwise wall shear stress initially increases due to local acceleration of the bulk flow, then abruptly declines beyond

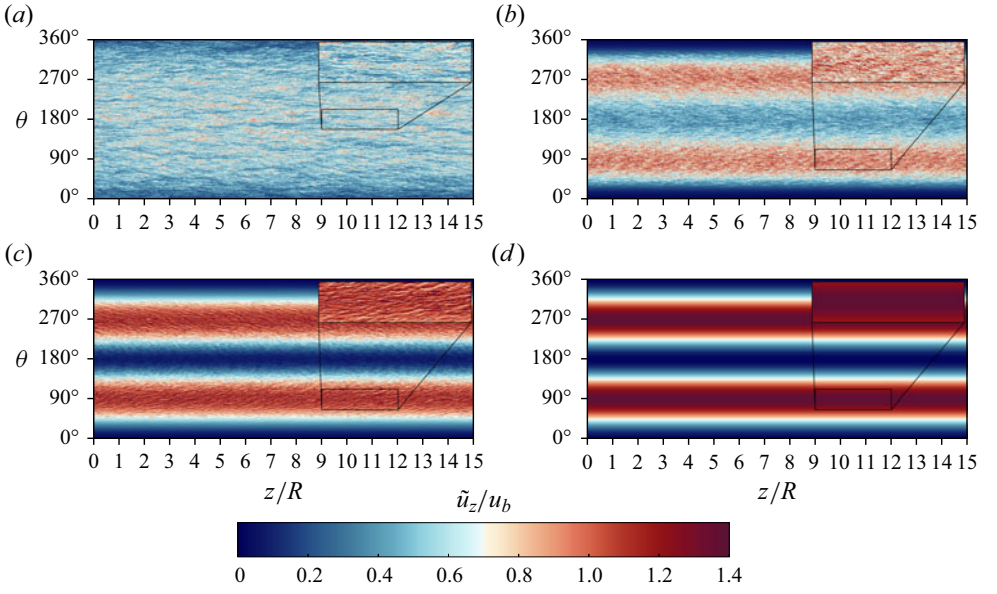

Figure 5. Instantaneous axial velocity (u_z/u_b) at $Re_b = 133\,000$ in an unrolled cylindrical shell at a distance $y^* = 15$ from the wall (evaluated in the non-rotating case). Contour levels ranging from 0 to 1.4 are shown, in colour scale from blue to red. The insets in the top-right corner of each panel report magnified views of a small portion of the shell. Various rotation numbers are considered: (*a*) $N = 0.01$, (*b*) $N = 0.5$, (*c*) $N = 2.0$, (*d*) $N = 16.0$.

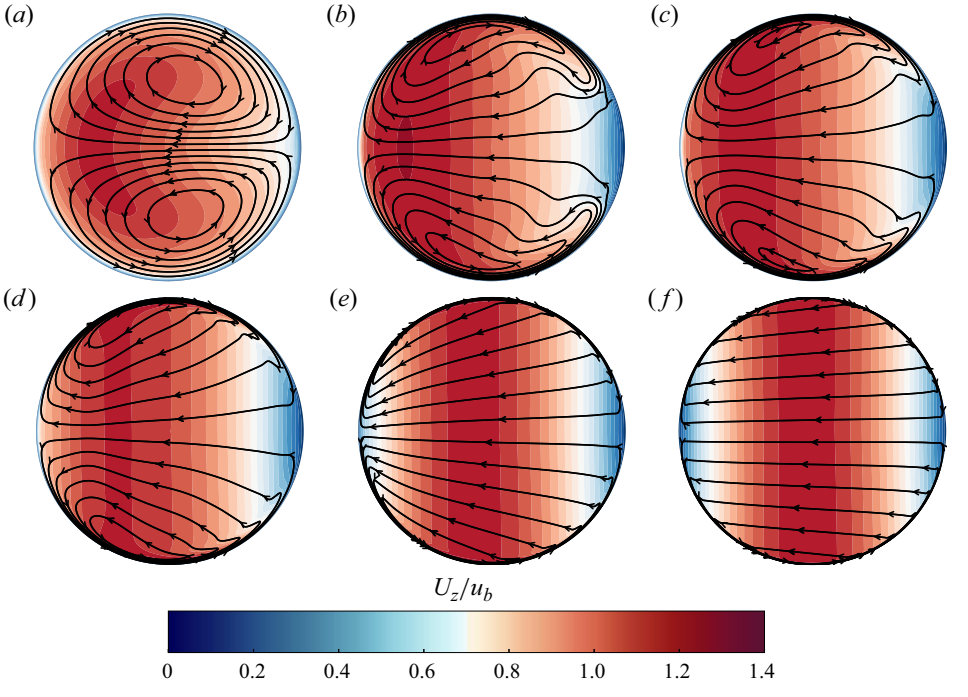

Figure 6. Mean axial velocity contours with superposed cross-flow streamlines, at $Re_b = 17\,000$. Twenty-four contour levels ranging from 0 to 1.4 are shown, in colour scale from blue to red. The pressure side of the pipe is on the left and the suction side is on the right of each panel. Various rotation numbers are considered: (*a*) $N = 0.0078125$, (*b*) $N = 0.125$, (*c*) $N = 0.25$, (*d*) $N = 0.5$, (*e*) $N = 2.0$, (*f*) $N = 8.0$.

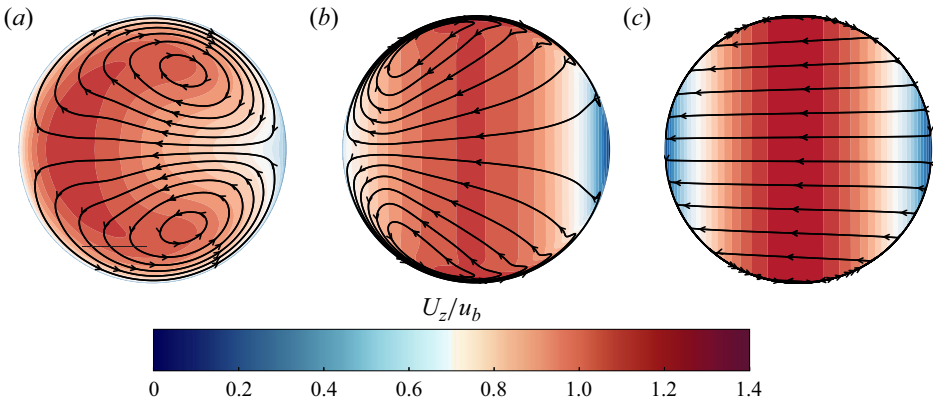

Figure 7. Mean axial velocity contours with superposed cross-flow streamlines, at $Re_b = 133\,000$. Twenty-four contour levels ranging from 0 to 1.4 are shown, in colour scale from blue to red. The pressure side of the pipe is on the left and the suction side is on the right of each panel. Various rotation numbers are considered: (*a*) $N = 0.01$, (*b*) $N = 0.5$, (*c*) $N = 16.0$.

$N \approx 1$, signifying the dominance of rotation and the concentration of momentum around the vertical axis of the pipe. Friction at the poles of the pipe ($\theta = 90^\circ, 270^\circ$) exhibits a monotonically increasing trend with the rotation number, on account of local thinning of the boundary layer, as detailed further ahead. At higher values of N considered, the local friction tends to attain a universal distribution when scaled by its mean value, regardless of the Reynolds number.

The mean axial velocity profiles are shown in outer scaling in figure 9. For the sake of clarity, the radial profiles are shown in the interval $\theta = [0, 90^\circ]$ along the pipe perimeter. Due to flow symmetry, this interval is sufficient to fully describe the state of the axial velocity in the pipe. The axial velocity for the non-rotating case ($N = 0$) is also reported for reference, which is obviously symmetric. As rotation sets in, the velocity profile along the horizontal symmetry axis (in orange shades) is immediately broken, and the peak value is shifted from the pipe centre to the pressure side of the pipe due to the presence of secondary motions in the cross-stream direction. The tendency of the axial velocity peak to shift towards the pressure side of the pipe is, however, non-monotonic. As the rotation number approaches unity, in fact the peak value of the axial velocity moves back towards the centre of the pipe, as shown in figure 9(*b–d*), and the velocity profiles again become symmetric with respect to the origin. As for the velocity profiles along the polar direction (in purple shades), they show a sudden tendency to flatten out in the middle of the pipe, whereas peaks tend to arise towards the pipe walls, which are associated with the formation of Ekman layers due to rotation. This tendency is exacerbated at high N, at which the mean axial velocity is very nearly constant throughout the vertical axis of the pipe, and gradients become progressively restricted to the near-wall vicinity. This change in the flow structure is clearly related to the onset of Taylor–Proudman columns previously noted when discussing figure 6. The same changes in the flow behaviour are also observed at $Re_b = 133\,000$ (figure 9(*e–h*). However, when comparing cases with the same vale of N (e.g. figures 9*b* and 9*f*), one can observe that the tendency for the flow to become symmetric about the vertical axis is faster at higher Re_b, whereas the Ekman layers are visually thinner at the higher Re_b.

It is important to recognise the substantial difference of the present flow arrangement with respect to the case of a spanwise rotating channel which was considered by

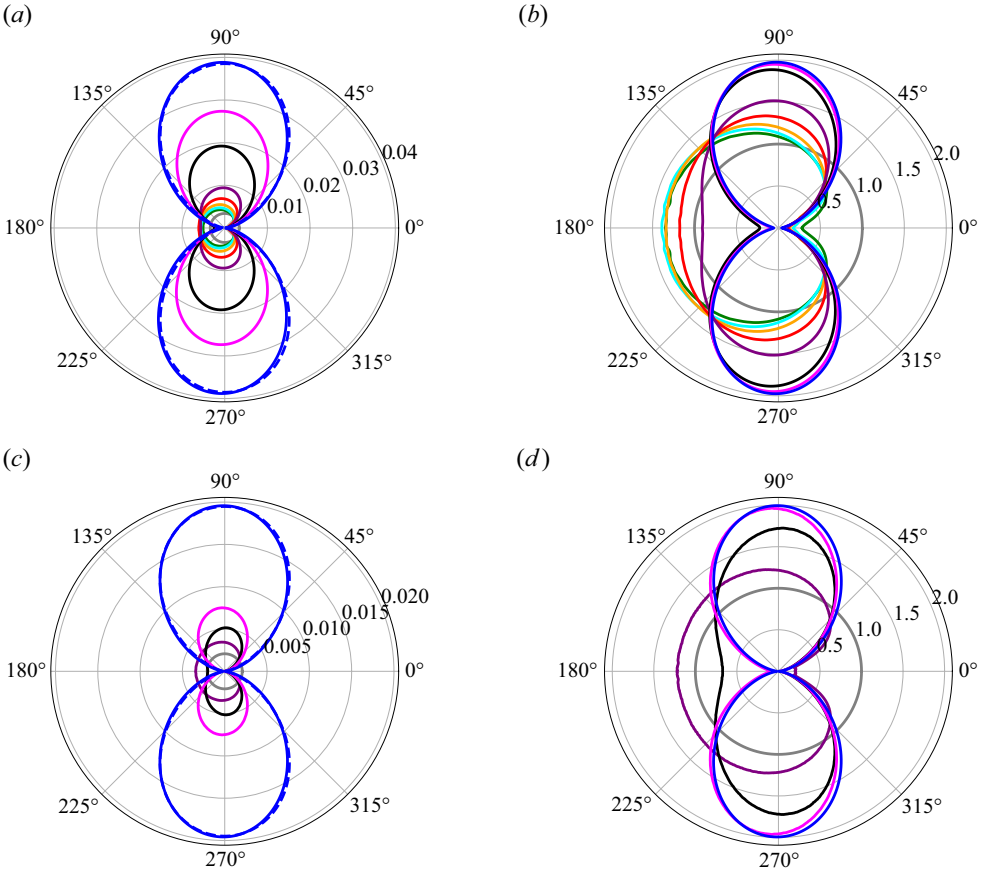

Figure 8. Polar distribution of the local streamwise wall shear stress (τ_w), normalised by either the reference dynamic pressure ρu_b^2 (*a*,*c*) or the mean wall shear stress τ_w^* (*b*,*d*), at $Re_b = 17\,000$ (*a*,*b*) and $Re_b = 133\,000$ (*c*,*d*). The colour codes correspond to different values of N, as given in table 1, grey denoting cases without rotation. The dashed blue line in (*a*,*c*) denotes the predictive formula given in (5.4).

Kristoffersen & Andersson (1993). In that case the Taylor–Proudman columns that would form at high rotation rates would be aligned with the spanwise direction, parallel to the rotation axis. Hence, they would not interact with solid walls and give rise to Ekman layers, which in the flow case under scrutiny here are chiefly responsible for drag increase around the north and south poles, as figure 8 shows.

Figure 10 reports representative wall-normal axial velocity profiles in local wall units (i.e. based on the local friction velocity $u_\tau = (\tau_w/\rho)^{1/2}$) as a function of the wall distance, to highlight deviations from the universal law of the wall which is observed in non-rotating pipe flow. For the sake of clarity, the velocity profiles are shown up to the occurrence point of their first maximum. The figure shows that the velocity distributions on the suction side (orange shades) become immediately diverted from the logarithmic behaviour, highlighting a clear decrease of the local friction. The velocity profiles on the pressure side (in cyan shades) are more resilient to the effect of rotation, and a logarithmic layer is still observed at low rotation numbers. At intermediate rotation numbers, the logarithmic part of the velocity profiles is shifted downwards, indicating an increase of the local friction, until the logarithmic layer becomes entirely disrupted at $N \gtrsim 1$. As seen in Figure 10(*e*–*h*),

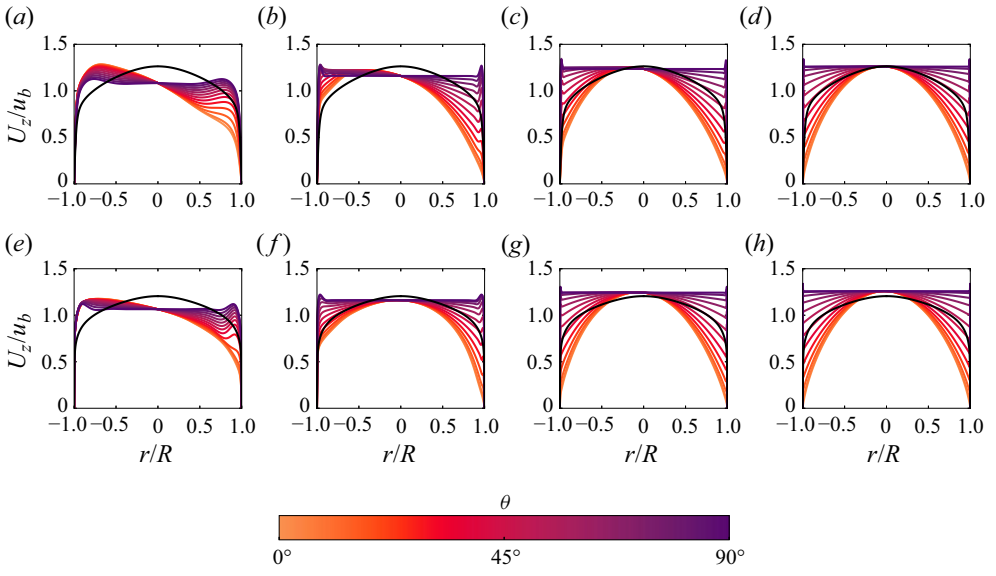

Figure 9. Radial profiles of outer-scaled axial velocity at various azimuthal positions, for flow cases at $Re_b = 17\,000$ (*a–d*) and $Re_b = 133\,000$ (*e–h*). Only the interval $\theta = [0°, 90°]$ is shown, at stations spaced 7.5° apart, with negative values of r signifying profiles taken at $\theta + 180°$. Values of (*a*) $N = 0.03125$, (*b*) $N = 0.5$, (*c*) $N = 2.0$, (*d*) $N = 8.0$, (*e*) $N = 0.1$, (*f*) $N = 0.5$, (*g*) $N = 2.0$, (*h*) $N = 16.0$. The black solid line denotes the mean axial velocity profile in the non-rotating case.

an increase of the Reynolds number mainly implies greater robustness of the logarithmic behaviour, which persists until $N \approx 1$ at $Re_b = 133\,000$.

Yang *et al.* (2020) argued that, for a channel that rotates about its spanwise axis at a reasonably high speed, the mean flow near the pressure side should follow a linear scaling, i.e.

$$U_z^+ = 2\frac{\Omega y}{u_\tau} + C, \tag{3.1}$$

with additive constant

$$C = \frac{1}{\kappa}\log\left(\frac{u_\tau^2}{\nu\Omega}\right). \tag{3.2}$$

This prediction is compared with the DNS data in figure 11, where we have assumed $\kappa = 0.33$. We find that the scaling holds with reasonable accuracy for cases with intermediate rotation rate, specifically for $N = 0.25, 0.5$ at $Re_b = 17\,000$ and for $N = 0.5, 2.0$ at $Re_b = 133\,000$, but it clearly fails at high rotation rates as the flow relaminarises.

The statistics of the turbulence kinetic energy ($k = \langle u_i u_i \rangle/2$) are examined in figure 12. As for the mean velocity, we find that axial symmetry observed in non-rotating cases is broken in the presence of weak rotation. At low rotation numbers (figure 12*a*) the magnitude of the buffer-layer peak along the horizontal symmetry axis of the pipe (orange shades) increases on the pressure side and decreases on the suction side, in response to increase and decrease of the imposed shear, respectively. Relaminarisation of the flow occurs on the suction side of the pipe already at $N \approx 0.125$. The buffer-layer peaks along the polar direction (purple shades) are instead barely affected. The most notable feature in the weak rotation regime is the reduction and flattening of k in the interior part of the pipe. This tendency becomes most evident as N increases, with suppression of the

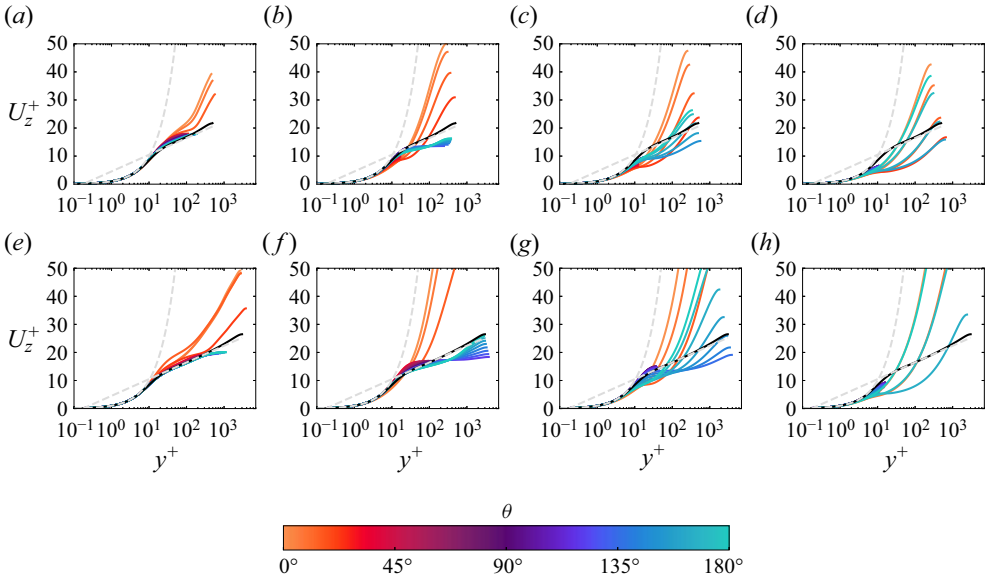

Figure 10. Wall-normal profiles of inner-scaled axial velocity, at various azimuthal positions spaced 7.5° apart, for flow cases at $Re_b = 17\,000$ (*a–d*) and $Re_b = 133\,000$ (*e–h*). Only the interval $\theta = [0°, 180°]$ is shown. Values of (*a*) $N = 0.03125$, (*b*) $N = 0.5$, (*c*) $N = 2.0$, (*d*) $N = 8.0$, (*e*) $N = 0.1$, (*f*) $N = 0.5$, (*g*) $N = 2.0$, (*h*) $N = 16.0$. The black solid line denotes the mean axial velocity profile in the non-rotating case. The dashed grey lines depict the compound law of the wall $U^+ = y^+$, $U^+ = \log y^+/0.387 + 4.53$.

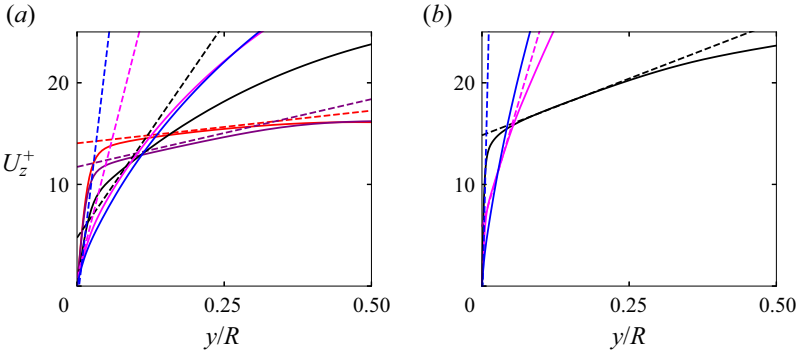

Figure 11. Inner-scaled wall-normal mean velocity profiles at $\theta = 180°$ (pressure side). Solid lines refer to DNS data and dashed lines to (3.1), for flow cases at $Re_b = 17\,000$ (*a*) and cases at $Re_b = 133\,000$ (*b*). Colour codes are as in table 1.

turbulence kinetic energy in the entire flow field, at $N \gtrsim 2$. A similar scenario is also found at higher Re_b (figure 12*e–h*), at which, however, some signs of turbulence activity are still visible at the pressure side, even at $N = 2$ (figure 12*g*). The flow is found to be fully laminar at $N = 16$.

As noted when discussing figure 9, starting from rotation numbers of the order of unity, the flow exhibits the clear hallmark of Ekman layers, namely thin layers in which the direction of the wall-parallel velocity changes as a result of varying relative importance of imposed pressure gradient, Coriolis and viscous forces. The laminar Ekman solution for

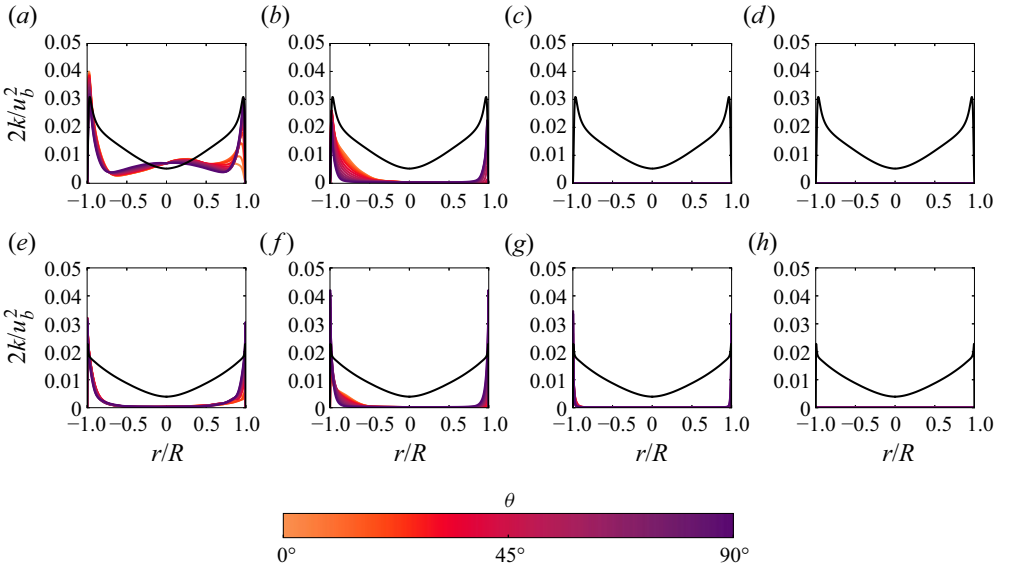

Figure 12. Radial profiles of outer-scaled turbulence kinetic energy at various azimuthal positions, for flow cases at $Re_b = 17\,000$ (*a–d*) and $Re_b = 133\,000$ (*e–h*). Only the interval $\theta = [0°, 90°]$ is shown, at stations spaced 7.5° apart, with negative values of r signifying profiles taken at $\theta + 180°$. Values of (*a*) $N = 0.03125$, (*b*) $N = 0.5$, (*c*) $N = 2.0$, (*d*) $N = 8.0$, (*e*) $N = 0.1$, (*f*) $N = 0.5$, (*g*) $N = 2.0$, (*h*) $N = 16.0$. The black solid line denotes the mean turbulence kinetic energy profile in the non-rotating case.

rotating flow over a flat wall reads (Greenspan 1968)

$$\frac{U_z(y)}{U_g} = 1 - \mathrm{e}^{-y/\Delta}\cos\left(\frac{y}{\Delta}\right), \tag{3.3a}$$

$$\frac{U_\theta(y)}{U_g} = \mathrm{e}^{-y/\Delta}\sin\left(\frac{y}{\Delta}\right), \tag{3.3b}$$

where y is the wall distance, U_g is the intensity of the asymptotic (geostrophic) wind and $\Delta = (\nu/\Omega)^{1/2}$ is the thickness of the Ekman layer. The Ekman layer in the vicinity of the north pole of the pipe (namely $\theta = 90°$) is analysed in figure 13, where the wall distance is scaled with respect to the Ekman length scale, and the geostrophic wind intensity is assumed to be the mean velocity at the pipe centreline, say U_0. The individual axial and azimuthal velocity components are shown in figure 13(*a*), the flow angle with respect to the axial direction is shown in figure 13 (*b*) and the projection in the hodograph plane is shown in figure 13 panel (*c*). As the rotation number increases the figure shows the onset of an overshoot of the axial velocity and the presence of a non-zero azimuthal velocity component. As a consequence, the flow becomes diverted from the axial direction, to an extent which is proportional to N. Excellent agreement between the computed profiles at high values of the rotation number and the theoretical prediction given in (3.3) is found. This is in our opinion a rather remarkable result, as the laminar Ekman solution is derived for the case of wall-normal rotation over a flat wall. Here, we find that it also applies with excellent accuracy to flow over a curved surface, with an effective rotation rate given by the wall-normal projection of the angular velocity vector. The same arguments apply for the highest tested Reynolds number (see figure 14), for which a laminar Ekman layer is found at $N = 16$.

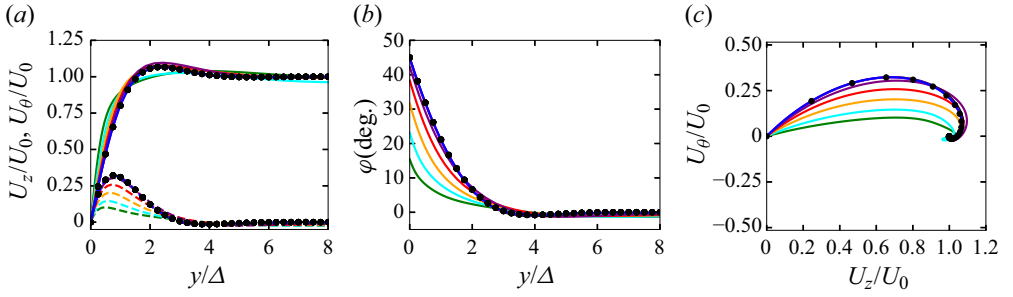

Figure 13. Profiles of mean axial (U_z) and azimuthal (U_θ) velocity (a), wall-parallel flow angle $\varphi = \tan^{-1}(U_\theta/U_z)$ (b) and hodograph diagram (c) at the polar coordinate $\theta = \pi/2$ (north pole of the pipe). Data are shown for $Re_b = 17\,000$, at various rotation numbers: $N = 0.03125$, $N = 0.0625$, $N = 0.125$, $N = 0.25$, $N = 0.5$, $N = 2.0$, $N = 4.0$, $N = 8.0$. See table 1 for the colour codes. The velocity profiles are scaled by the mean centreline axial velocity U_0. The black circles denote the analytical solution for a laminar Ekman layer (Greenspan 1968).

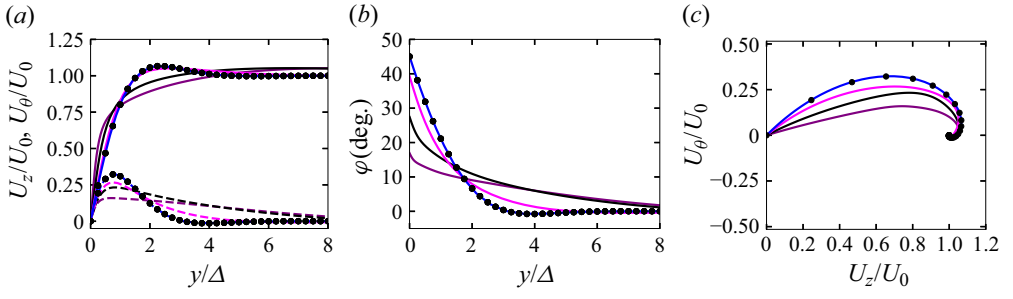

Figure 14. Profiles of mean axial (U_z) and azimuthal (U_θ) velocity (a), wall-parallel flow angle $\varphi = \tan^{-1}(U_\theta/U_z)$ (b) and hodograph diagram (c) at the polar coordinate $\theta = \pi/2$ (north pole of the pipe). Data are shown for $Re_b = 133\,000$, at various rotation numbers: $N = 0.1$, $N = 0.5$, $N = 2.0$, $N = 16.0$. See table 1 for the colour codes. The velocity profiles are scaled by the mean centreline axial velocity U_0. The black circles denote the analytical solution for a laminar Ekman layer (Greenspan 1968).

4. Friction

Frictional drag in pipes is obviously a parameter of paramount importance as it is related to power expenditure to sustain the flow. Whereas accurate estimates of friction are available for pressure-driven pipe flow, the presence of imposed rotation has profound effects on the structure of turbulence and the onset of secondary motions, which were pinpointed in the previous section. In order to isolate the contributions of turbulence, secondary motions and rotation to frictional drag, here we consider a generalised version of the FIK identity (Fukagata, Iwamoto & Kasagi 2002), which was derived for flow in ducts with arbitrary cross-section (Modesti *et al.* 2018). The starting point is the mean momentum balance equation, which reads

$$\nu\nabla^2 U_z = -\Pi + \boldsymbol{\nabla}\cdot\boldsymbol{\tau_T} + \boldsymbol{\nabla}\cdot\boldsymbol{\tau_C} + F_{c,z}, \tag{4.1}$$

where Π is the driving pressure gradient, $\boldsymbol{\tau_T} = \langle u_z \boldsymbol{u_{r\theta}}\rangle$ accounts for turbulent convection ($\boldsymbol{u_{r\theta}} = (u_r, u_\theta)$ is the cross-stream velocity vector), $\boldsymbol{\tau_C} = U_z \boldsymbol{U_{r\theta}}$ accounts for mean cross-stream convection (hence, with the secondary motions) and $F_{c,z}$ is the axial component of the Coriolis forces given in (2.1). Equation (4.1) may be regarded as a Poisson equation for U_z velocity whose source terms can be obtained from DNS data.

Hence, the mean streamwise velocity field can be cast as a superposition of four contributions, which individually satisfy

$$\nabla^2 U_{zV} = -\Pi, \quad \nabla^2 U_{zT} = \boldsymbol{\nabla} \cdot \boldsymbol{\tau_T}, \quad \nabla^2 U_{zC} = \boldsymbol{\nabla} \cdot \boldsymbol{\tau_C}, \quad \nabla^2 U_{zR} = F_{c,z}, \quad (4.2a\text{–}d)$$

with homogeneous boundary conditions, from viscous effects (V), from turbulence (T), from mean cross-stream convection (C) and from rotation (R). The bulk velocity can then be obtained as the superposition of four terms,

$$u_b = u_{bV} + u_{bT} + u_{bC} + u_{bR}, \quad (4.3)$$

each denoting the mean value associated with the four velocity fields defined in (4.2*a–d*). Using (4.3) in the definition of the friction factor one obtains

$$\lambda = \frac{8\tau_w^*}{\rho u_{bV} u_b}\left(1 - \frac{u_{bT}}{u_b} - \frac{u_{bC}}{u_b} - \frac{u_{bR}}{u_b}\right) = \lambda_V + \lambda_T + \lambda_C + \lambda_R, \quad (4.4)$$

where the viscous contribution ($\lambda_V = 64/Re_b$) corresponds to the case of laminar flow. This information has major importance as it allows one to highlight the key physical mechanisms for friction generation depending on the pipe rotation rate. Notably, (4.4) reverts to the classical FIK identity in the case of canonical plane channel and circular pipe flow, in the absence of rotation. It is important to acknowledge that the FIK identity cannot be strictly intended as a tool to precisely isolate causality links in the flow. For instance, it is clear that secondary motions in circular pipe flow would not form in the absence of rotation, and that rotation causes a change in the structure of turbulence. Nevertheless, the generalised form of the FIK identity as here introduced is useful as it provides quantitation of the friction contributions from the various terms appearing in the mean momentum balance equation, thus allowing one to identify distinct flow regimes depending on their relative importance.

Figure 15 shows the contributions to the mean friction factor in both relative and absolute terms. According to (4.4), the absolute viscous contribution to the friction factor does not change with N, hence its relative contribution decreases monotonically. As regards the turbulent contribution, in non-rotating cases it increases from 86 % (at $Re_b = 17\,000$) to 97 % (at $Re_b = 133\,000$), and it monotonically decreases with N, becoming negligible at $N \gtrsim 1$. At the lower Re, for which several data points are available at low N, we see that the contributions to friction are basically identical to those for the non-rotating case up to $N \approx 0.001$. The contribution from the secondary motions has a non-monotonic behaviour being nearly zero in the two extreme cases of non-rotating and rapidly rotating flow, whereas it accounts for as much as 50 % in the intermediate rotation regimes ($0.01 \leqslant N \leqslant 0.1$). The distributions are also very similar at the two Reynolds numbers reported in the figure, although λ_C is found to become slightly negative at the higher Re. This similarity might suggest that N is an appropriate parameter to quantify the importance of secondary motions in radially rotating pipe flow. Monotonic growth of the contribution due to rotation is observed, with weak sensitivity to the Reynolds number. In quantitative terms, rotation accounts for almost 40 % of the total friction for $N \approx 0.1$, and it is responsible for at least 80 % of friction at $N \gtrsim 1$.

5. Friction estimates

Based on the results of the previous section, herein we attempt to derive predictive formulas for the friction coefficient as a function of the controlling parameters, namely Reynolds and rotation numbers. Preliminarily, we consider the two limiting cases of no

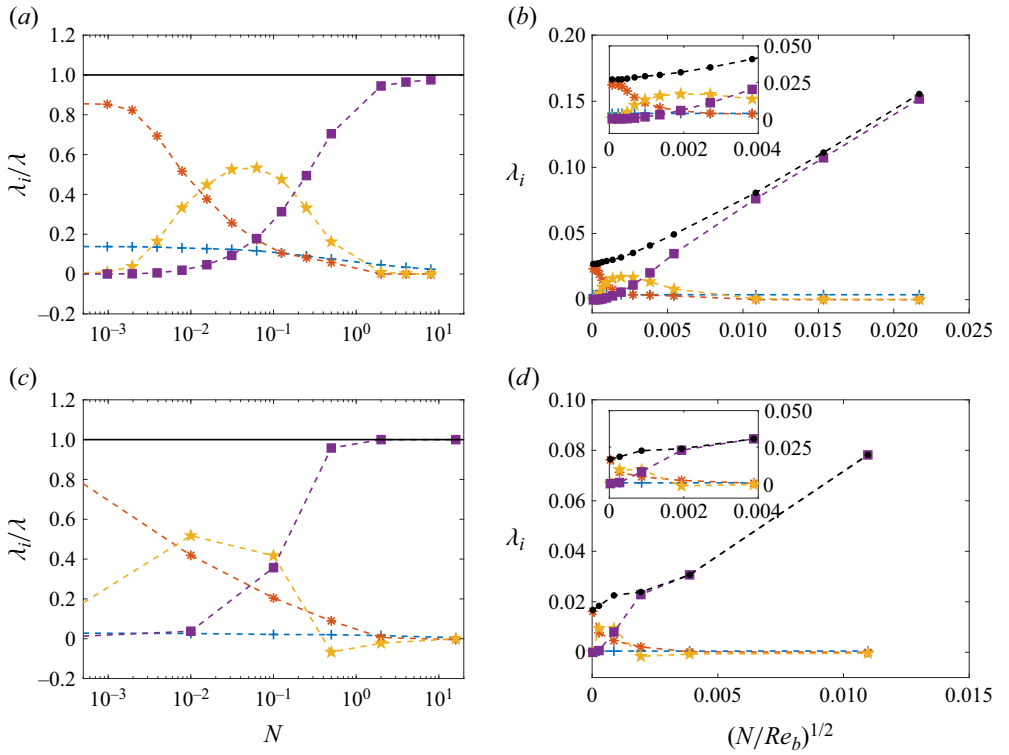

Figure 15. Contributions to friction factor (•) from viscous effects (+), turbulence (∗), mean cross-stream convection (★) and rotation (■), as defined in (4.4). Percentage contributions are shown as a function of N in (*a*,*c*) and absolute contributions are shown as a function of $(N/Re_b)^{1/2}$ in (*b*,*d*), for $Re_b = 17\,000$ (*a*,*b*) and $Re_b = 133\,000$ (*c*,*d*).

rotation ($N = 0$) and rapid rotation ($N \gg 1$). In the former case, the Prandtl friction law for smooth pipes is known to perform very well, namely

$$1/\lambda_0^{1/2} = A \log_{10}\left(Re_b \lambda_0^{1/2}\right) - B, \tag{5.1}$$

where λ_0 is the friction factor for the non-rotating case at a given Re_b, and $A \approx 2.102$, $B \approx 1.148$, as obtained from fitting DNS data (Pirozzoli *et al.* 2021).

In the opposite case of rapid rotation an approximate theoretical treatment is possible as the flow tends to become fully laminar. As a first step for that purpose, we recall that analysis of the mean velocity maps in figures 6 and 7 shows that, with the exception of the near-wall Ekman layers, the mean axial velocity becomes solely a function of the horizontal direction as a result of the Taylor–Proudman theorem. Hence, in figure 16 we show a scatter plot of the mean axial velocity as a function of the horizontal coordinate ($x_1 = r\cos\theta$), after removing points closer to the wall than 5Δ, which roughly corresponds to the effective thickness of the Ekman layer. The figure shows that, regardless of the Reynolds number, all data points fall on the same distribution, thus corroborating the initial assumption. Furthermore, we find that a convenient fit for the axial velocity distribution is as follows:

$$\frac{U_{z,e}(r,\theta)}{u_b} = A\left[1 - \left(\frac{r}{R}\right)^2 \cos^2\theta\right] + B\left[1 - \left(\frac{r}{R}\right)^2 \cos^2\theta\right]^2, \tag{5.2}$$

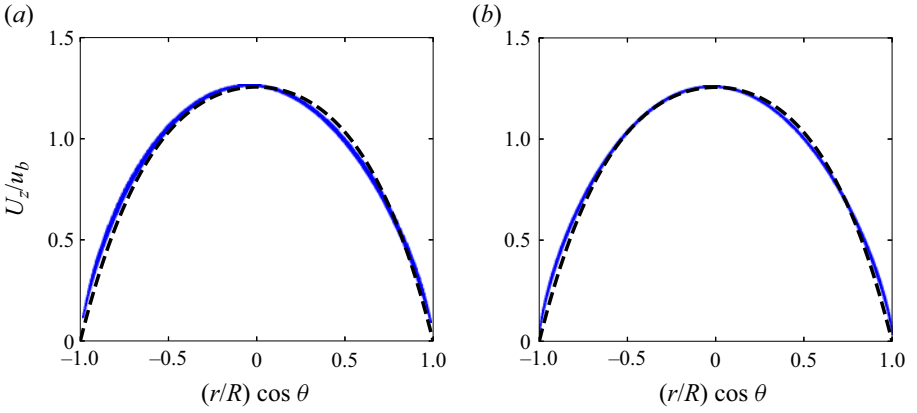

Figure 16. Scatter plots of mean axial velocity as a function of the horizontal coordinate, for $Re_b = 17\,000$, $N = 8$ (*a*) and $Re_b = 133\,000$, $N = 16$ (*b*), in blue. Only points at wall distance greater than five Ekman layer thicknesses are shown. The black dashed lines denote the velocity profile given in (5.2).

with $A = 1.74$ and $B = -0.484$ as determined from fitting the DNS data, which also lends itself to simple mathematical manipulations. Lack of perfect symmetry in figure 16 is rather apparent, which could be incorporated in (5.2); however, the practical impact of such corrections on the overall friction would be minimal.

As for the mean axial velocity profiles within the Ekman layer, (3.3*a*) is adapted to the present case by assuming that: (i) the local effective angular velocity at a given azimuthal angle is the wall-normal component, namely $\Omega \sin\theta$, and (ii) the effective geostrophic velocity is the wall-limiting value of the mean velocity distribution in the pipe core, as given in (5.2); hence we set $U_g(\theta) = U_{z,e}(R, \theta)$.

These assumptions are scrutinised in figure 17, where we shown the mean axial velocity profiles as a function of the wall distance, scaled respectively by the assumed geostrophic velocity and by the local Ekman layer thickness. Several profiles along the pipe perimeter are shown, with the exception of those at $\theta = 0^\circ$ and $\theta = 180^\circ$, where $U_{z,e} = 0$. The cases with highest rotation numbers for each extreme Reynolds number are reported in the figure. The figure confirms that the local Ekman layer thickness ($\Delta = (\nu/(\Omega \sin\theta))^{1/2}$) is the correct length scale for the velocity profiles, as it yields universality of the velocity overshoot point, which occurs at $y \approx 2.3\Delta$, regardless of the azimuthal positions. Whereas the profiles near the north pole, $\theta = 90^\circ$, exhibit perfect agreement with the canonical Ekman solution, good agreement is also observed at all azimuthal positions.

A prediction for the distribution of the wall friction along the pipe perimeter is then obtained from (3.3*a*), which upon differentiation at the wall yields

$$\frac{\tau_w}{\rho} = \nu \frac{\mathrm{d}U_z}{\mathrm{d}y}\bigg|_{y=0} = \nu \frac{U_{z,e}(R,\theta)}{(\nu/(\Omega \sin\theta))^{1/2}}. \tag{5.3}$$

Using (5.2) to determine the geostrophic velocity one then obtains

$$\tau_w = 2^{1/2}\rho u_b^2 (\sin\theta)^{1/2} \left(\frac{N}{Re_b}\right)^{1/2} \left[A\left(1-\cos^2\theta\right) + B\left(1-\cos^2\theta\right)^2\right]. \tag{5.4}$$

This prediction is tested in figure 8 (dashed blue line in figure 8*a*,*c*) for the cases at the highest rotation number, for which it is found to yield an excellent approximation of the

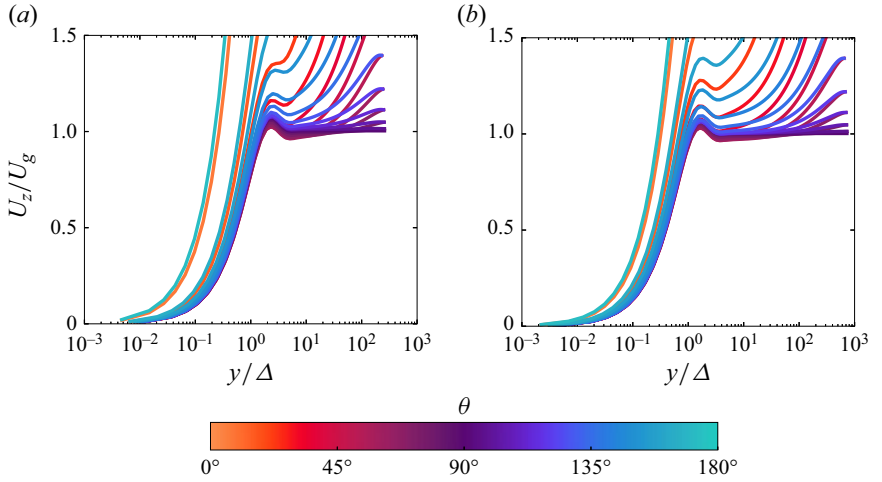

Figure 17. Mean axial velocity profiles scaled by the local geostrophic velocity (U_g) as a function of wall distance normalised by the local Ekman layer thickness, $\Delta = (\nu/(\Omega \sin\theta))^{1/2}$, at $Re_b = 17\,000$, $N = 8$ (a) and $Re_b = 133\,000$, $N = 16$ (b). Profiles along the pipe perimeter are shown in intervals of 7.5°, with the exception of $\theta = 0°$ and $\theta = 180°$.

DNS data. Finally, the global friction factor is evaluated by averaging the wall shear stress (5.4) along the pipe perimeter to obtain

$$\lambda = \frac{8\tau_w^*}{\rho u_b^2} = \frac{8}{\rho u_b^2}\frac{1}{2\pi}\int_0^{2\pi} \tau_w \,\mathrm{d}\theta = k_E \left(\frac{N}{Re_b}\right)^{1/2}, \tag{5.5}$$

with $k_E \approx 7.044$ resulting from integration.

This is the key prediction of the present study, which implies that the similarity parameter for friction in the rapidly rotating pipe regime is N/Re_b. This prediction is in line with the analysis of Pallares *et al.* (2005), who derived a similar scaling for the friction coefficient at the lateral walls of rotating square ducts. It is important to acknowledge that, at high rotation rates ($N \gtrsim 1$), friction basically only includes the viscous and rotational contributions, hence to a good approximation

$$\lambda = \frac{64}{Re_b} + k_E \left(\frac{N}{Re_b}\right)^{1/2}. \tag{5.6}$$

Figure 18(a) compares the prediction of (5.6) with the DNS data at various N, Re_b. The agreement is remarkably good provided $(N/Re_b)^{1/2} \geqslant 0.005$.

In light of the previously noted flow complexity, cases with intermediate rotation can only be handled via semi-empirical formulas. For instance, to achieve continuous transition from the non-rotating case to the rapidly rotating regime, we propose the following interpolation:

$$\lambda = \left(\lambda_0^2 + k_E^2 \frac{N}{Re_b}\right)^{1/2}, \tag{5.7}$$

with λ_0 defined in (5.1). It is noteworthy to mention that this type of blending already includes the viscous contribution to the friction through the non-rotating part λ_0. The results of the proposed interpolation formula are shown in figure 18(b) which indicate

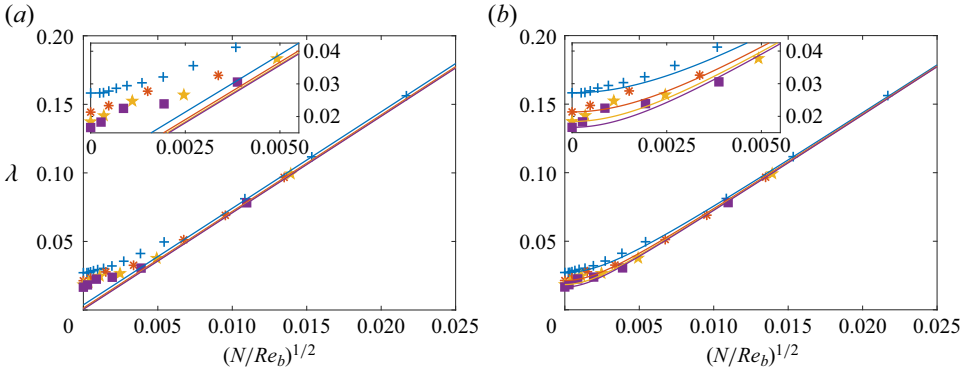

Figure 18. Distribution of friction factor as a function of $(N/Re_b)^{1/2}$ for DNS data at $Re_b = 17\,000$ (+), $Re_b = 44\,000$ (∗), $Re_b = 82\,500$ (★), $Re_b = 133\,000$ (■). In (*a*), the solid lines denote the asymptotic prediction for the rapid-rotation regime (5.6) at $Re_b = 17\,000$ (blue), $Re_b = 44\,000$ (red), $Re_b = 82\,500$ (orange), $Re_b = 133\,000$ (purple). Lines in (*b*) denote prediction of the interpolation formula (5.7).

reasonable prediction of the friction factor. However, the DNS data may exhibit complex non-monotonic behaviour (e.g. see the figure inset), which is not accounted for by (5.7).

A popular semi-empirical formula correlation for the intermediate-rotation regime was proposed by Ito & Nanbu (1971). According to their study, the similarity parameter for friction in the turbulent regime is $K_t = Re_b N^2/4$; hence they proposed that, for $1 \leqslant K_t \leqslant 500$,

$$\frac{\lambda}{\lambda_0} = 0.942 + 0.058 K_t^{0.282}, \tag{5.8}$$

whereas at $K_t > 500$ one should use

$$\frac{\lambda}{\lambda_0} = 0.924 K_t^{0.05}. \tag{5.9}$$

In figure 19 we compare these empirical formulas with the DNS data. Use of the parameter K_t indeed yields satisfactory universality of the friction data in the range of modest rotation numbers, at which friction increase with respect to the non-rotating case is no more than 30 %; however, discrepancies at high rotation rates are very large. In this range of parameters the correlation of Ito & Nanbu (1971) is consistent with the DNS data, but not quantitatively accurate. We find that a marginally better empirical fit is given by the power-law formula

$$\frac{\lambda}{\lambda_0} = 1.09 K_t^{0.033}. \tag{5.10}$$

As shown in figure 19(*b*), this formula is more accurate at low values of K_t. Analysis of the zoomed inset within figure 18(*b*) reveals a non-trivial trend of the friction factor within the Reynolds number range from 44 000 to 133 000. Notably, at the lowest rotation rates the friction factor exhibits steeper growth than given in (5.7), which leads us to suggest the correlation (5.10) in that regime, although it may also fail if the parameter K_t drops below 0.01, as the agreement is not perfect there.

6. Conclusions

Numerical investigation of flow in a rotating pipe through DNS has revealed a rather complex scenario, which includes disparate flow regimes, whose occurrence

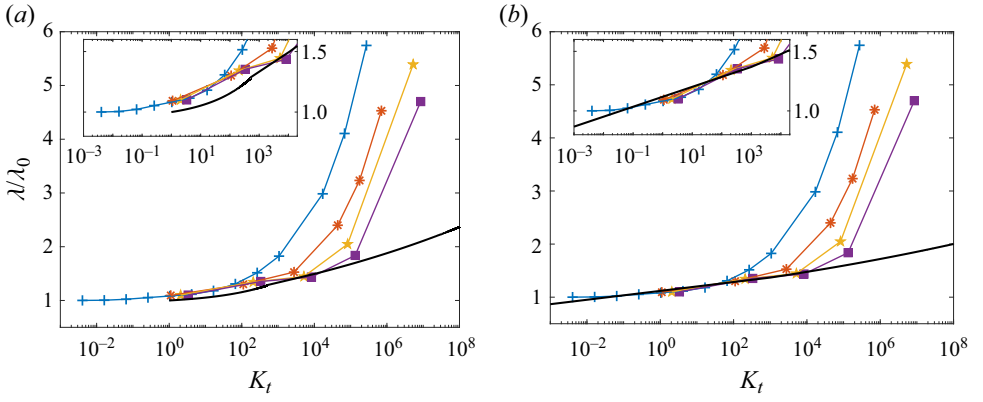

Figure 19. Distribution of friction factor (normalised by the non-rotating case value) as a function of the parameter $K_t = Re_b N^2/4$ (Ito & Nanbu 1971) for DNS data at $Re_b = 17\,000$ (+), $Re_b = 44\,000$ (∗), $Re_b = 82\,500$ (★), $Re_b = 133\,000$ (■). In (*a*), the black line denotes the composite correlation (5.8) + (5.9), and in (*b*) the power-law fit (5.10).

critically depends on the delicate balance between rotational, inertial and viscous forces. In particular, in contrast to the case of flow in a non-rotating pipe, we have observed strong inhomogeneity of the flow along the azimuthal direction, with local flow features being primarily controlled by the rotation number. Specifically, at low rotation numbers, the flow features strong asymmetry between the pressure side, where turbulence intensifies and the local friction coefficient increases, and the suction side, where turbulence is significantly suppressed, even under very modest rotation rates. In this regime, the poles of the pipe aligned with the rotation axis are relatively unaffected. As a result, friction increases mildly as compared with the non-rotating case, at a rate which is reasonably well predicted by the correlation (5.10), which is an improvement over empirical formulas proposed in previous studies based on experimental campaigns (Ito & Nanbu 1971). At higher rotation numbers, the effects of rotation manifest themselves more clearly with the formation of Taylor–Proudman columns, with accumulation of momentum in the central part of the pipe, and return to a symmetric state, whereby the pressure side of the pipe also tends to attain a laminar state, along with the rest of the flow. In this regime the flow features a core region with flow properties depending only on the direction normal to the angular velocity, and thin laminar Ekman layers adjacent to the walls, across which the magnitude and the flow direction change abruptly. The most important observation based on the DNS data is that the wall-normal velocity profiles within the Ekman layers at a given azimuthal coordinate are very accurately parametrised in terms of the local wall-normal projection of the angular velocity with associated viscous length scale, and of the local value of the core velocity. This finding allows a boundary-layer-like theory to be developed and applied for the prediction of the local and global friction coefficients. The analysis highlights the crucial importance of the parameter N/Re_b in controlling the fast-rotation regime of motion. Indeed, in agreement with studies for square ducts (Pallares *et al.* 2005), we find that $\lambda \sim (N/Re_b)^{1/2}$, hence the friction factor increases with the rotation number at much faster rate than in the low-N regime.

In the case of low-to-moderate rotation number the friction factor has a complex behaviour resulting from the interplay of viscosity, turbulence, secondary motions and Coriolis forces, which we have rigorously isolated and distilled in an extended form of the FIK identity. In general terms, the analysis shows decreasing importance of turbulence

and increasing importance of Coriolis forces at increasing rotation number, with a cross-over at $N \approx 0.1$, where the effect of secondary motions is also maximum. Hence, we have identified three flow regimes: (1) a low-rotation-rate regime in which the momentum budget is essentially the same as in non-rotating flow, for $N \lesssim 0.001$; (2) an intermediate-rotation-rate regime for $0.001 \lesssim N \lesssim 1$, for which all physical effects convey a comparable contribution to the friction factor; and (3) a high-rotation-rate regime for $N \gtrsim 1$, for which the contributions of Coriolis and viscous forces are by far dominant. The intermediate-rotation regime is especially challenging as all physical effects are at play, thus precluding analytical quantification. However, empirical power-law correlations such as that by Ito & Nanbu (1971) can provide reasonably accurate prediction of friction, upon suitable tuning of the coefficients.

We anticipate that these insights into the effect of rotation on frictional drag will have significant implications for the design and operation of engineering applications where controlling or leveraging rotational effects is essential. Given the substantial role of secondary motions in the intermediate-rotation regime (contributing up to 50 % of total friction), we also recognise that accurately predicting these effects presents a considerable challenge for turbulence models. The present database offers a valuable benchmark for developing improved models.

Supplementary material. Supplementary movies are available at https://doi.org/10.1103/APS.DFD.2023.GFM.V0041. The data that support the findings of this study are openly available at http://newton.dma.uniroma1.it/database.

Acknowledgements. We acknowledge the CINECA award under the ISCRA initiative and EuroHPC Joint Undertaking for the availability of high-performance computing resources and support. The authors thank Dr M. Yu for the insightful exchange of ideas regarding the topic of the paper.

Funding. S.P. acknowledges financial support from ICSC – Italian Research Center on High Performance Computing, Big Data and Quantum Computing – Spoke 6, funded by European Union – NextGenerationEU (CUP B83C22002830001). A.C. acknowledges financial support from Sapienza University under 'Add SAPIExcellence Fellowship 2024'.

Declaration of interests. The authors report no conflict of interest.

Author ORCIDs.
Alessandro Ceci https://orcid.org/0000-0001-6664-1677;
Sergio Pirozzoli https://orcid.org/0000-0002-7160-3023.

Appendix

Given the complex nature of the flow under scrutiny we have carried out a comprehensive study of the effect of the pipe length and grid resolution on the flow statistics. General guidelines for the selection of the grid spacings in wall-bounded flows were provided by Hoyas & Jiménez (2006), namely that the streamwise spacing should be $\Delta z^+ \lesssim 10$, the spanwise spacing should be $R^+\Delta\theta \lesssim 5$ and the wall-normal spacing at the wall should be $\Delta r_w^+ \ll 1$. Figure 20 reports the azimuthal distribution of the grid spacings for all flow cases herein computed. In cases with low rotation rate and fully turbulent flow, the previous prescriptions are in fact satisfied. However, these putative upper bounds are exceeded in flows with high rotation rate. This observation could convey the false impression that the DNS are under-resolved, whereas it is rather associated with the occurrence of a locally laminar flow state, to which the traditional estimates do not apply. For complex flows such as the one under scrutiny here only a grid resolution study, which we report hereafter, can provide guidance for the selection of grid and computational box size. For that purpose, a

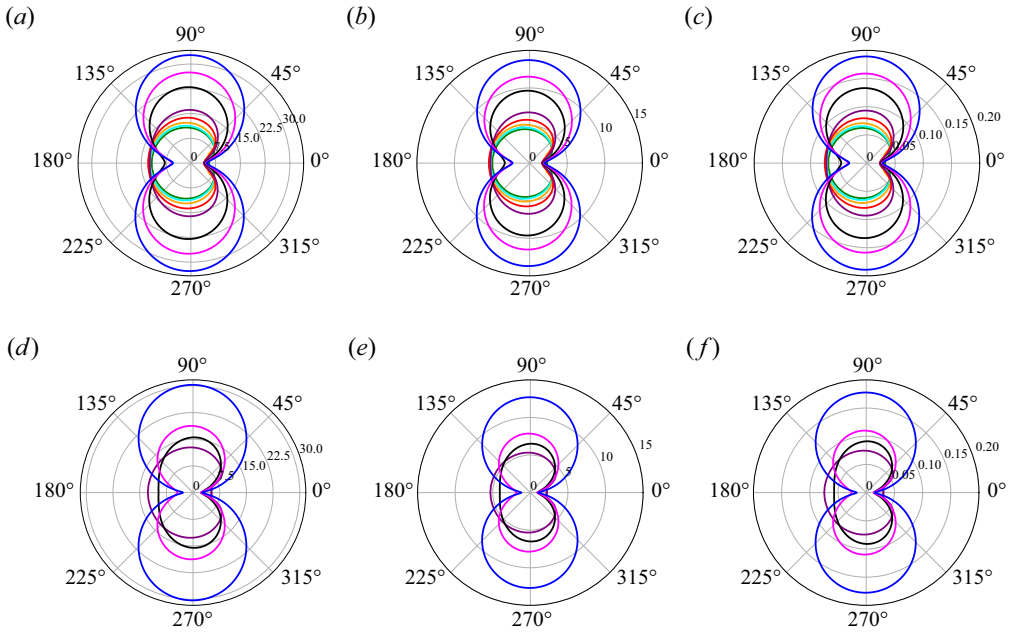

Figure 20. Polar distribution of the inner-scaled grid spacings, at $Re_b = 17\,000$ (*a–c*) and $Re_b = 133\,000$ (*d–f*): streamwise spacing Δz^+ (*a*,*d*), azimuthal spacing $R^+\Delta\theta$ (*b*,*e*) and radial spacing at the wall Δr_w^+ (*c*,*f*). The colour codes correspond to different values of N, as given in table 1.

Re_b	Re_τ	N	L_z/R	$N_z \times N_r \times N_\theta$	$\lambda \times 10^{-2}$	Line
17 000	669	0.5	15	769 × 97 × 769	4.963	
17 000	669	0.5	30	1537 × 97 × 769	4.963	
17 000	669	0.5	45	2305 × 97 × 769	4.963	
17 000	670	0.5	15	769 × 193 × 769	4.977	
17 000	669	0.5	15	769 × 97 × 1537	4.966	

Table 2. Computational parameters for grid sensitivity study. See table 1 for the nomenclature.

representative flow case with moderate rotation rate has been considered, namely $Re_b = 17\,000$, $N = 0.5$.

A summary of the relevant simulations we have carried out is given in table 2, whereby we have doubled or tripled the pipe length, and doubled the number of grid points along the azimuthal and radial directions. As a first confirmation that grid convergence of the statistics is achieved, the table shows differences of no more than 0.3 % in the global friction coefficient, as compared with the baseline simulation. This conclusion is corroborated from figure 21, showing the azimuthal distribution of the local streamwise wall shear stress. Again, the influence of pipe length (figure 21*a*) and grid resolution (figure 21*b*) is seen to be negligible, showing overall relative differences smaller than 0.6 % for cases with finer grids. Last, in figure 22 we show the outer-scaled velocity profiles in the wall-normal direction. The profiles are found to be identical on the suction side and only exhibit small differences (of less than 0.7 %) on the pressure side for cases with finer grids.

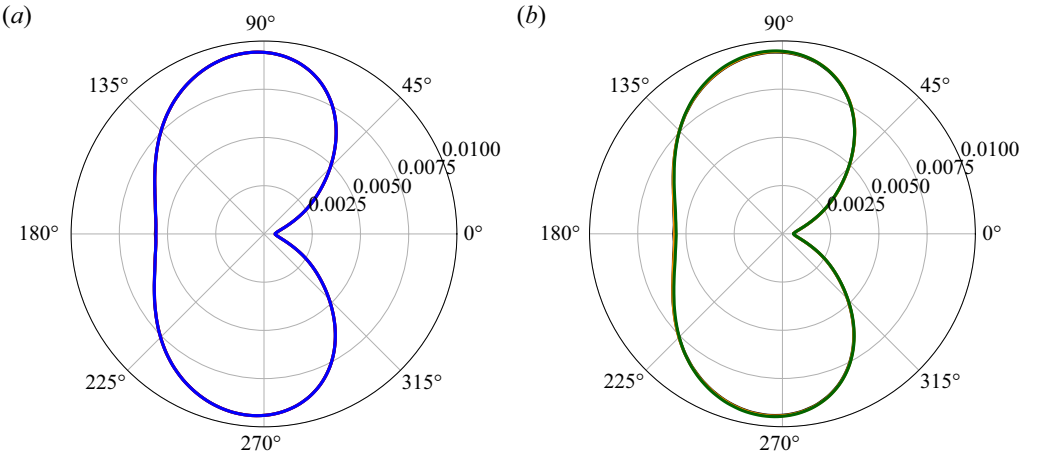

Figure 21. Polar distribution of the local streamwise wall shear stress (τ_w) normalised by the reference dynamic pressure ρu_b^2 at $Re_b = 17\,000$ and $N = 0.5$. (*a*) Effects of domain length and (*b*) effects of grid refinement. The colour codes correspond to the different runs of the grid sensitivity study, as given in table 2.

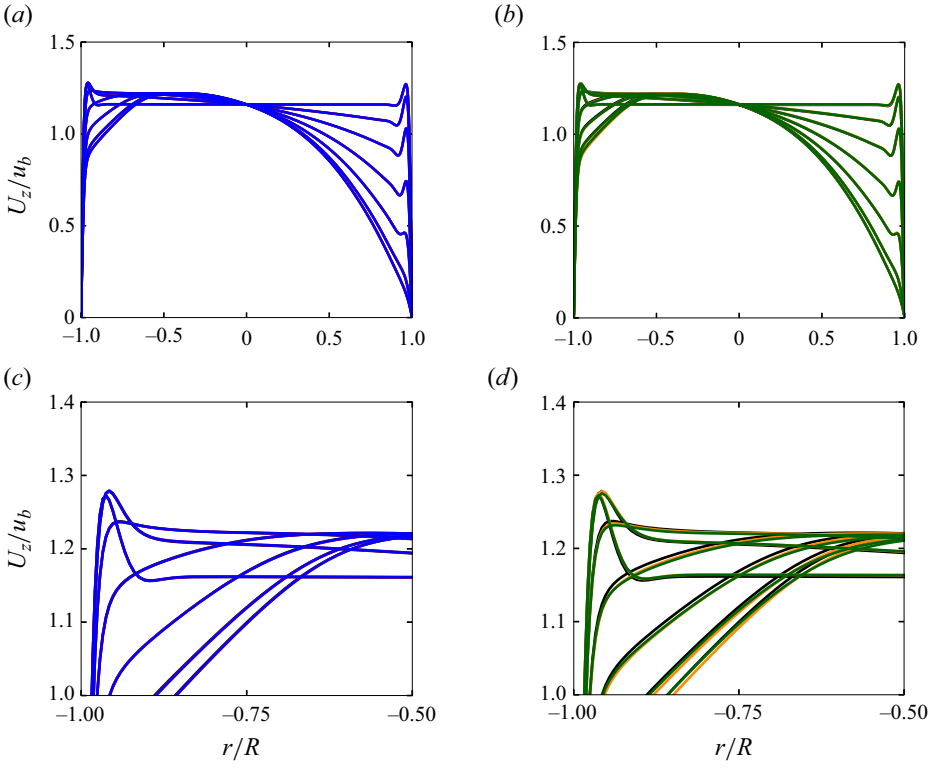

Figure 22. Radial profiles of outer-scaled axial velocity at various azimuthal positions for flow cases at $Re_b = 17\,000$ and $N = 0.5$. Only the interval $\theta = [0°, 90°]$ is shown, at stations spaced 15° apart, with negative values of r signifying profiles taken at $\theta + 180°$. (*a*,*c*) Effects of pipe length and (*b*,*d*) effects of grid refinement. The colour codes correspond to the different runs of the grid sensitivity study, as given in table 2.

References

Akselvoll, K. & Moin, P. 1996 An efficient method for temporal integration of the Navier–Stokes equations in confined axisymmetric geometries. *J. Comput. Phys.* **125**, 454–463.

Atkins, N.R. & Kanjirakkad, V. 2014 Flow in a rotating cavity with axial throughflow at engine representative conditions. In *Turbo Expo: Power for Land, Sea, and Air, Volume 5C: Heat Transfer*, p. V05CT16A041. ASME.

Barua, S.N. 1954 Secondary flow in a rotating straight pipe. *Proc. R. Soc. Lond.* A **227**, 133–139.

Benton, G.S. & Boyer, D. 1966 Flow through a rapidly rotating conduit of arbitrary cross-section. *J. Fluid Mech.* **26**, 69–79.

Coletti, F., Jacono, D.L., Cresci, I. & Arts, T. 2014 Turbulent flow in rib-roughened channel under the effect of coriolis and rotational buoyancy forces. *Phys. Fluids* **26** (4), 045111.

Coletti, F., Maurer, T., Arts, T. & Di Sante, A. 2012 Flow field investigation in rotating rib-roughened channel by means of particle image velocimetry. *Exp. Fluids* **52**, 1043–1061.

Dai, Y.-J., Huang, W.-X., Xu, C.-X. & Cui, G.-X. 2015 Direct numerical simulation of turbulent flow in a rotating square duct. *Phys. Fluids* **27**, 065104.

Fang, X., Yang, Z., Wang, B.-C. & Bergstrom, D.J. 2017 Direct numerical simulation of turbulent flow in a spanwise rotating square duct at high rotation numbers. *Intl J. Heat Fluid Flow* **63**, 88–98.

Fatica, M. & Ruetsch, G. 2014 *CUDA Fortran for Scientists and Engineers*. Elsevier.

Fukagata, K., Iwamoto, K. & Kasagi, N. 2002 Contribution of Reynolds stress distribution to the skin friction in wall-bounded flows. *Phys. Fluids* **14**, L73–L76.

Greenspan, H.P. 1968 *The Theory of Rotating Fluids*. Cambridge University Press.

Greitzer, E.M., Tan, C.S. & Graf, M.B. 2007 *Internal Flow: Concepts and Applications*. Cambridge University Press.

Hoyas, S. & Jiménez, J. 2006 Scaling of velocity fluctuations in turbulent channels up to $Re_\tau = 2003$. *Phys. Fluids* **18**, 011702.

Ishigaki, H. 1996 Analogy between turbulent flows in curved pipes and orthogonally rotating pipes. *J. Fluid Mech.* **307**, 1–10.

Ito, H. & Nanbu, K. 1971 Flow in rotating straight pipes of circular cross section. *Trans. ASME J. Basic Engng* **93**, 383–394.

Jackson, R.W., Luberti, D., Tang, H., Pountney, O.J., Scobie, J.A., Sangan, C.M., Owen, J.M. & Lock, G.D. 2021 Measurement and analysis of buoyancy-induced heat transfer in aero-engine compressor rotors. *Trans. ASME J. Engng Gas Turbines Power* **143** (6), 061004.

Johnston, J.P., Halleent, R.M. & Lezius, D.K. 1972 Effects of spanwise rotation on the structure of two-dimensional fully developed turbulent channel flow. *J. Fluid Mech.* **56**, 533–557.

Kim, J. & Moin, P. 1985 Application of a fractional-step method to incompressible Navier–Stokes equations. *J. Comput. Phys.* **59**, 308–323.

Kristoffersen, R. & Andersson, H.I. 1993 Direct simulations of low-Reynolds-number turbulent flow in a rotating channel. *J. Fluid Mech.* **256**, 163–197.

Ligrani, P. 2013 Heat transfer augmentation technologies for internal cooling of turbine components of gas turbine engines. *Intl J. Rot. Machin.* **2013**, 275653.

Liou, T.-M., Chang, S.-W., Hung, J.-H. & Chiou, S.-F. 2007 High rotation number heat transfer of a 45 rib-roughened rectangular duct with two channel orientations. *Intl J. Heat Mass Transfer* **50** (19–20), 4063–4078.

Luberti, D., Patinios, M., Jackson, R.W., Tang, H., Pountney, O.J., Scobie, J.A., Sangan, C.M, Owen, J.M. & Lock, G.D. 2021 Design and testing of a rig to investigate buoyancy-induced heat transfer in aero-engine compressor rotors. *Trans. ASME J. Engng Gas Turbines Power* **143** (4), 041030.

Mårtensson, G., Gunnarsson, J., Johansson, A.V. & Moberg, H. 2002 Experimental investigation of a rapidly rotating turbulent duct flow. *Exp. Fluids* **33**, 482–487.

Modesti, D., Pirozzoli, S., Orlandi, P. & Grasso, F. 2018 On the role of secondary motions in turbulent square duct flow. *J. Fluid Mech.* **847**, R1.

Morris, W.D. 1996 A rotating facility to study heat transfer in the cooling passages of turbine rotor blades. *Proc. Inst. Mech. Engrs* **210** (1), 55–63.

Orlandi, P. 2000 *Fluid Flow Phenomena: A Numerical Toolkit*. Kluwer.

Pallares, J. & Davidson, L. 2000 Large-eddy simulations of turbulent flow in a rotating square duct. *Phys. Fluids* **12**, 2878–2894.

Pallares, J., Grau, F.X. & Davidson, L. 2005 Pressure drop and heat transfer rates in forced convection rotating square duct flows at high rotation rates. *Phys. Fluids* **17**, 075102.

Pirozzoli, S. & Orlandi, P. 2021 Natural grid stretching for dns of wall-bounded flows. *J. Comput. Phys.* **439**, 110408.

PIROZZOLI, S., ROMERO, J., FATICA, M., VERZICCO, R. & ORLANDI, P. 2021 One-point statistics for turbulent pipe flow up to $Re_\tau \approx 6000$. *J. Fluid Mech.* **926**, A28.

PROUDMAN, J. 1916 On the motion of solids in a liquid possessing vorticity. *Proc. R. Soc. Lond.* A **92** (642), 408–424.

ROSAS, R.H., ZHANG, Z.-P. & WANG, B.-C. 2021 Direct numerical simulation of turbulent elliptical pipe flow under system rotation about the major axis. *Phys. Rev. Fluids* **6** (8), 084609.

SUN, Z., GAO, F., CHEW, J.W & AMIRANTE, D. 2022 Large eddy simulation investigation of low Rossby number buoyant flow in rotating cavities. *Trans. ASME J. Engng Gas Turbines Power* **144** (12), 121023.

TAYLOR, G.I. 1917 Motion of solids in fluids when the flow is not irrotational. *Proc. R. Soc. Lond.* A **93** (648), 99–113.

VERZICCO, R. & ORLANDI, P. 1996 A finite-difference scheme for three-dimensional incompressible flows in cylindrical coordinates. *J. Comput. Phys.* **123**, 402–414.

VISSCHER, J., ANDERSSON, H.I., BARRI, M., DIDELLE, H., VIBOUD, S., SOUS, D. & SOMMERIA, J. 2011 A new set-up for PIV measurements in rotating turbulent duct flows. *Flow Meas. Instrum.* **22** (1), 71–80.

WU, X. & MOIN, P. 2008 A direct numerical simulation study on the mean velocity characteristics in turbulent pipe flow. *J. Fluid Mech.* **608**, 81–112.

YANG, X.I.A., XIA, Z.-H., LEE, J., LV, Y. & YUAN, J. 2020 Mean flow scaling in a spanwise rotating channel. *Phys. Rev. Fluids* **5**, 074603.

ZHANG, Z.-P. & WANG, B.-C. 2019 Direct numerical simulation of turbulent flow in a circular pipe subjected to radial system rotation. *Flow Turbul. Combust.* **103**, 1057–1079.